Chinese Chemical Letters 35 (2024) 108421

Contents lists available at ScienceDirect

Chinese Chemical Letters

journal homepage: www.elsevier.com/locate/cclet

Mitigating the dissolution of V_2O_5 in aqueous $ZnSO_4$ electrolyte through Ti-doping for zinc storage

Zihe Wei[a,b,c], Xuehua Wang[c], Ting Zhu[b], Ping Hu[b,d,*], Liqiang Mai[a,b,d], Liang Zhou[a,b,d,*]

[a] Hubei Longzhong Laboratory, Wuhan University of Technology (Xiangyang Demonstration Zone), Xiangyang 441000, China
[b] State Key Laboratory of Advanced Technology for Materials Synthesis and Processing, Wuhan University of Technology, Wuhan 430070, China
[c] School of Materials Science and Engineering, Wuhan Institute of Technology, Wuhan 430205, China
[d] Foshan Xianhu Laboratory of the Advanced Energy Science and Technology Guangdong Laboratory, Xianhu Hydrogen Valley, Foshan 528200, China

ARTICLE INFO

Article history:
Received 3 February 2023
Revised 20 March 2023
Accepted 2 April 2023
Available online 5 April 2023

Keywords:
Aqueous zinc-ion batteries
V_2O_5 cathode materials
Aqueous $ZnSO_4$ electrolyte
Yolk-shell structure
Ti doping

ABSTRACT

Aqueous zinc-ion batteries (AZIBs) have become a hotspot for electrochemical energy storage owing to the high safety, low cost, environmental friendliness, and favorable rate performance. However, the serious dissolution of cathode materials in aqueous electrolytes would lead to poor cyclability, which should be addressed before commercialization. Herein, we designed a Ti-doped V_2O_5 with yolk-shell microspherical structure for AZIBs. The Ti doping stabilizes the crystal structure and relieves the dissolution of V_2O_5 in aqueous $ZnSO_4$ electrolyte. The optimized sample, $Ti_{0.2}V_{1.8}O_{4.9}$, delivers a high capacity (355 mAh/g at 0.05 A/g) as well as good capacity retention (89% after 2500 cycles at 1.0 A/g). This work provides an effective strategy to mitigate the dissolution of cathode material in aqueous $ZnSO_4$ electrolyte for cyclability enhancement.

Gradual replacement of fossil fuels with renewable energy is an inevitable trend for alleviating energy depletion and environmental pollution. However, most renewable energy such as solar and wind are intermittent. Developing reliable energy storage technologies is able to overcome the intermittency issue [1,2]. Aqueous zinc-ion battery (AZIB) represents a competitive technology for large scale energy storage because of the high theoretical capacity (820 mAh/g) as well as low redox potential (−0.76 V *vs.* standard hydrogen electrode) of Zn [3]. The mild and near-neutral aqueous electrolytes enable unique advantages of non-flammability, low cost, environmental friendliness, fast charging/discharging capability, and easy assembly of AZIBs [4–7].

A series of cathode materials have been proposed for AZIBs, including manganese oxides [8–12], vanadium oxides [13–18], prussian blue analogs [19,20], and organic compounds [21,22]. Among these materials, vanadium oxides attract special attentions due to the high capacity, rich crystal structures, and variable valence states. Take the layered vanadium pentoxide (V_2O_5) as an example, it possesses an ultrahigh theoretical capacity of 589 mAh/g [23]. However, it suffers from poor cycling stability due to the dissolution of vanadium oxide in aqueous $ZnSO_4$ electrolytes [24,25]. To improve the cyclability, efforts have been devoted to morphology engineering, electrolyte modification, and intercalating foreign ions/molecules into the layered structure, which are able to reduce the dissolution and stabilize the crystal structure [26–28]. For example, Yang *et al.* found that V_2O_5 hollow spheres outperformed commercial V_2O_5 in cyclability and rate performance due to the higher surface area of V_2O_5 hollow spheres [29]. Temple-free yolk-shell V_2O_5 demonstrated a high capacity and ideal reversibility owing to the volume expansion alleviating ability of yolk-shell structure [30–32]. Pre-intercalating various metal ions (Na^+, Mg^{2+}, Ni^{2+}, Zn^{2+}, *etc.*) and crystalline water into layered V_2O_5 could enlarge the interlayer spacings for Zn^{2+} transfer and storage [33–37]. For example, with an enlarged interlayer spacing for Zn^{2+} transfer, Ca^{2+}-preintercalated V_2O_5 manifests high capacity, decent rate performance, and long cycling life [38]. In most of these studies, the improved electrochemical performances were achieved with high-price $Zn(CF_3SO_3)_2$ or $Zn(TFSI)_2$ electrolytes. Improving the electrochemical performance of V_2O_5 in low-cost aqueous $ZnSO_4$ electrolyte has been rarely reported [39–41].

Herein, we synthesize Ti-doped V_2O_5 yolk-shell microspheres (TVO) with tunable Ti content by a spray-drying method. 3.0 mol/L $ZnSO_4$ is used as the electrolyte to explore the effects of Ti doping on electrochemical performance. The yolk-shell TVO mitigates the dissolution of vanadium in aqueous electrolyte and buffers the volume change during Zn^{2+} intercalation/de-intercalation. The yolk-shell $Ti_{0.2}V_{1.8}O_{4.9}$ delivers a high capacity of 355 mAh/g at 0.05 A/g.

* Corresponding authors.
E-mail addresses: huping316@163.com (P. Hu), liangzhou@whut.edu.cn (L. Zhou).

https://doi.org/10.1016/j.cclet.2023.108421
1001-8417/

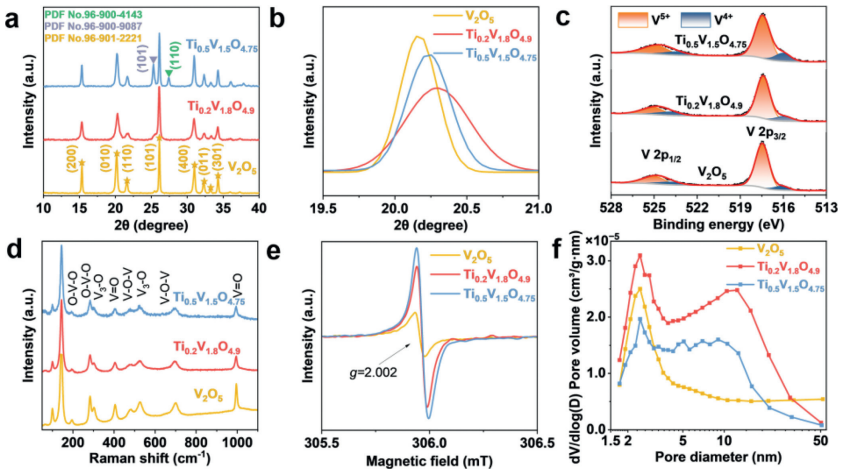

Fig. 1. (a, b) XRD patterns, (c) XPS spectra, (d) Raman spectra, (e) EPR spectra, and (f) pore size distributions of V_2O_5, $Ti_{0.2}V_{1.8}O_{4.9}$ and $Ti_{0.5}V_{1.5}O_{4.75}$.

When cycled at 1.0 A/g, 89% of the reversible capacity (211 mAh/g) can be retained after 2500 cycles. The *in-situ* and *ex-situ* characterizations reveal that the doping of an appropriate amount of Ti into the lattice of vanadium pentoxides stabilizes the crystal structure. Further increasing the Ti amount lowers the specific capacity due to the reduce of active material content. AZIB pouch cells based on the $Ti_{0.2}V_{1.8}O_{4.9}$ cathode and 3.0 mol/L $ZnSO_4$ electrolyte demonstrates good cyclability under deep charging and discharging conditions. Our research offered an effective means to extend the service life of AZIBs with low-cost aqueous $ZnSO_4$ electrolyte.

The TVO samples with different Ti contents are produced by a simple spray drying method with subsequent annealing in air. The $Ti_{0.2}V_{1.8}O_{4.9}$ displays an X-ray diffraction (XRD) pattern resembled to that of V_2O_5 (Fig. 1a). The characteristic peaks at 15.3°, 20.2°, 21.6°, 26.1°, 30.9°, 32.3°, 33.2° and 34.2° are associated with the (200), (010), (110), (101), (400), (011), (111) and (301) diffractions of the orthorhombic phase V_2O_5 (PDF No. 96–901–2221). For $Ti_{0.5}V_{1.5}O_{4.75}$, besides the diffractions from the V_2O_5 phase, additional obvious diffractions at 25.3° and 27.4° associated with the (101) plane of anatase TiO_2 (PDF No. 96–900–9087) and (110) plane of rutile TiO_2 (PDF No. 96–900–4143) can also be detected. The results indicate that doping a low content of Ti ($Ti/(Ti+V) \leq 10\%$) does not change the crystal structure of V_2O_5, while doping too much Ti (25%) leads to the formation of residue phases. The diffraction peaks located at 19.5°–21° are enlarged in Fig. 1b. For V_2O_5, the (010) diffraction peak is located at 20.17°. When 10% Ti is doped, the diffraction shifts to 20.29°, while it shifts back to 20.23° when the Ti content is increased to 25%. It should be mentioned that although the Ti^{4+} (61 pm) has a larger ionic radius than the V^{5+} (54 pm), both the $Ti_{0.2}V_{1.8}O_{4.9}$ and $Ti_{0.5}V_{1.5}O_{4.75}$ show a reduced (010) lattice spacing compared to V_2O_5, indicating the existence of tensile stress in the Ti-doped samples [42,43]. According to the Bragg equation ($d = n\lambda/2\sin\theta$), the (010) lattice spacing of V_2O_5, $Ti_{0.2}V_{1.8}O_{4.9}$, and $Ti_{0.5}V_{1.5}O_{4.75}$ are calculated to be 4.40, 4.37 and 4.38 Å, respectively (Table S1 in Supporting information). The grain size of the samples can be determined by Scherrer equation ($D = K\lambda/\beta\cos\theta$). The grain sizes for V_2O_5, $Ti_{0.2}V_{1.8}O_{4.9}$ and $Ti_{0.5}V_{1.5}O_{4.75}$ are determined to be 26.3, 17.9 and 22.7 nm, respectively. The XRD Rietveld refinement results of $Ti_{0.2}V_{1.8}O_{4.9}$ and $Ti_{0.5}V_{1.5}O_{4.75}$ are provided in Fig. S1, Tables S2 and S3 (in Supporting information). From the Rietveld refinement results, one can know that the doped-Ti occupies the V sites.

Fig. 1c presents the X-ray photoelectron spectroscopy (XPS) spectra of the samples. Both V^{4+} (515.9 and 523.8 eV) and V^{5+} (517.4 and 525.0 eV) exist in the three samples. The V^{4+} content is 12.43% in V_2O_5 and it increases with the increasing of Ti amount. For $Ti_{0.2}V_{1.8}O_{4.9}$ and $Ti_{0.5}V_{1.5}O_{4.75}$, the V^{4+} contents are 18.14% and 22.69%, respectively. The existence of V^{4+} suggests the formation of oxygen vacancies in the TVO samples to keep charge neutrality [44]. The V_2O_5, $Ti_{0.2}V_{1.8}O_{4.9}$, and $Ti_{0.5}V_{1.5}O_{4.75}$ show almost identical Raman spectra (Fig. 1d). The characteristic peaks at 478 and 697 cm^{-1} are corresponded to the bending vibration and stretching vibration of V-O-V bond. And the peaks at 405 and 994 cm^{-1} are associated with the V=O bonds [42,45]. To further study the effects of Ti doping, electron paramagnetic resonance (EPR) has been conducted. All three samples present a peak at $g = 2.002$ (Fig. 1e), suggesting the presence of oxygen vacancies. The signal increases obviously with Ti doping amount, demonstrating that the substitution of V^{5+} with Ti^{4+} is accompanied by the introduction of oxygen vacancies for charge compensation [46].

N_2 adsorption-desorption isotherms of the three samples (Fig. S2 in Supporting information) all match with IV-type isotherm with H3 hysteresis loop [47]. The V_2O_5 shows a pore size centered at ~2.4 nm, while the $Ti_{0.2}V_{1.8}O_{4.9}$ and $Ti_{0.5}V_{1.5}O_{4.75}$ show a bimodal pore size distribution (Fig. 1f). Table S4 shows the BET surface areas of the samples. The $Ti_{0.2}V_{1.8}O_{4.9}$ possesses the highest surface area (27.05 m^2/g), while the V_2O_5 and $Ti_{0.5}V_{1.5}O_{4.75}$ show surface areas of 18.54 and 15.85 m^2/g, respectively. As for the pore volume, the V_2O_5, $Ti_{0.2}V_{1.8}O_{4.9}$ and $Ti_{0.5}V_{1.5}O_{4.75}$ show pore volumes of 0.10, 0.08 and 0.04 cm^3/g, respectively.

Scanning electron microscope (SEM) images show that the obtained V_2O_5 (Fig. 2a and Fig. S3a in Supporting information) has a porous spherical structure built up with interconnected nanoparticles with sizes of 50–100 nm. Between the interconnected nanoparticles, there are rich large pores with sizes of tens of nanometres. From a broken microsphere, a porous yolk can be observed below the porous shell, demonstrating the yolk-shell structure. Transmission electron microscopy (TEM, Fig. 2b) further verifies the yolk-shell structure of V_2O_5. High-resolution TEM (HRTEM, Fig. 2c) image shows clear lattice fringes from the (010) planes of orthorhombic V_2O_5. High-angle annular dark-field scanning transmission electron microscopy (HAADF-STEM) image and the corresponding elemental mappings show that the yolk of yolk-shell V_2O_5 contains a hollow cavity in the center. Energy dispersive X-ray spectroscopy (EDS) elemental mappings (Fig. 2d) show that the V and O elements distribute homogeneously in the yolk-shell microspheres.

With the introduction of 10%–25% of Ti, the yolk-shell structure of the samples can be well maintained (Figs. 2e, f, i and j), while the large mesopores on the surface disappear. With the in-

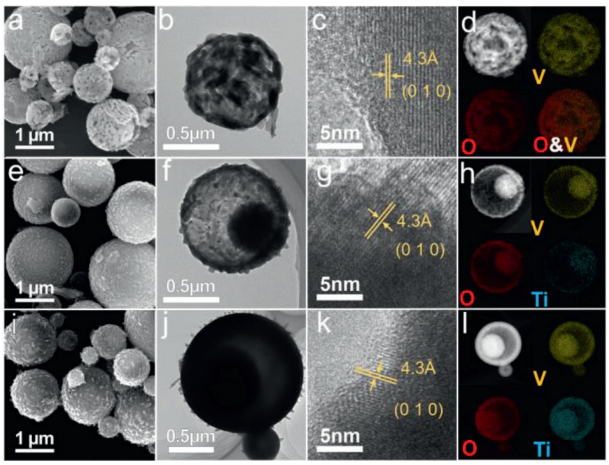

Fig. 2. (a) SEM image, (b) TEM image, (c) HRTEM image, and (d) EDS mappings of V_2O_5. (e) SEM image, (f) TEM image, (g) HRTEM image, and (h) EDS mappings of $Ti_{0.2}V_{1.8}O_{4.9}$. (i) SEM image, (j) TEM image, (k) HRTEM image, and (l) EDS mappings of $Ti_{0.5}V_{1.5}O_{4.75}$.

troduction of 10% Ti, the grain size of the sample decreases noticeably (Fig. S3b in Supporting information), agreeing well with the XRD results. Further increasing the Ti content from 10% to 25%, the grain size increases obviously (Fig. S3c in Supporting information), which is responsible for the decrease of surface area. Different from the yolk-shell V_2O_5 which possesses a hollow cavity in the yolk (Fig. 2b), both the $Ti_{0.2}V_{1.8}O_{4.9}$ and $Ti_{0.5}V_{1.5}O_{4.75}$ possess a solid spherical yolk (Figs. 2f and j). HRTEM confirms the high crystallinity of both $Ti_{0.2}V_{1.8}O_{4.9}$ (Fig. 2g) and $Ti_{0.5}V_{1.5}O_{4.75}$ (Fig. 2k). EDS elemental mappings (Figs. 2h and l) show that the Ti distribute homogeneously in the yolk-shell microspheres, demonstrating the successful doping.

To study the effect of Ti doping on the electrochemical performance, charge-discharge tests were performed in CR-2025 type coin cell with mild 3.0 mol/L $ZnSO_4$ electrolyte. Representative cyclic voltammetry (CV) curves of the samples are presented in Fig. S4 (Supporting information). The non-overlapping feature of CV profiles and gradual increasing of enclosed CV area indicate that all three samples experience a similar activation process. The transformations in peak position and peak intensity can be ascribed to the structure evolution of V_2O_5 to $Zn_xV_2O_5{\cdot}nH_2O$ during the cycling, which is common for vanadium oxide based cathode materials [48–50]. After five CV cycles, all three samples show two pairs of redox peaks at ~0.58/0.78 V and 0.87/1.15 V (Fig. 3a).

The galvanostatic charge discharge (GCD) curves of V_2O_5, $Ti_{0.2}V_{1.8}O_{4.9}$ and $Ti_{0.5}V_{1.5}O_{4.75}$ at 0.2 A/g are presented in Fig. 3b and Fig. S5 (Supporting information), and the cyclic performances of V_2O_5, $Ti_{0.2}V_{1.8}O_{4.9}$, and $Ti_{0.5}V_{1.5}O_{4.75}$ are presented in Fig. 3c. Agreeing with the CV profiles, all three samples experience an activation process during cycling (Fig. 3c). The activation process is caused by the gradual structural evolution from layered V_2O_5 to layered $Zn_xV_2O_5{\cdot}H_2O$ with expanded interlayer spacings [51–53]. After the activation process, the $Ti_{0.2}V_{1.8}O_{4.9}$ displays two discharge plateaus at ~0.6 and 0.9 V, corresponding to the Zn^{2+} intercalation. Upon cycling, the capacity of $Ti_{0.2}V_{1.8}O_{4.9}$ increases gradually until it reaches at ~250 mAh/g after ~25 cycles, after which the capacity decreases slightly. After 200 cycles at 0.2 A/g, the capacity retains at 211 mAh/g. Both the $Ti_{0.5}V_{1.5}O_{4.75}$ and V_2O_5 show quicker capacity fading after the activation process. When cycled at 1.0 A/g for 2500 cycles, the capacity retention of $Ti_{0.2}V_{1.8}O_{4.9}$ reaches 89.4% against the highest capacity, which is much higher than those of V_2O_5 (27.9%) and $Ti_{0.5}V_{1.5}O_{4.75}$ (43.9%) (Figs. 3d and e, Fig. S6 in Supporting information).

The GCD curves of V_2O_5, $Ti_{0.2}V_{1.8}O_{4.9}$ and $Ti_{0.5}V_{1.5}O_{4.75}$ under a serious of current densities (0.05–2.0 A/g) are shown in Fig. 3f and Fig. S7 (Supporting information). The discharge capacities of $Ti_{0.2}V_{1.8}O_{4.9}$ reach 341, 309, 282, 249, 222 and 187 mAh/g at 0.05, 0.1, 0.2, 0.5, 1.0 and 2.0 A/g, respectively. When the current density returns to 0.05 A/g, the capacity can be recovered to 298 mAh/g (Fig. 3g). Compared to the $Ti_{0.2}V_{1.8}O_{4.9}$, the V_2O_5 and $Ti_{0.5}V_{1.5}O_{4.75}$ exhibit lower capacities at the same current densities. The above results suggest that a proper amount of Ti doping can boost the cyclability as well as rate performance of V_2O_5.

Fig. 3h presents the electrochemical impedance spectroscopy (EIS) plots and the equivalent circuit is shown in Fig. S8 (Supporting information). The R_s and R_{ct} stands for the solution resistance and the charge transfer resistance between the electrode/electrolyte interface, respectively. The R_{ct} values of V_2O_5, $Ti_{0.2}V_{1.8}O_{4.9}$ and $Ti_{0.5}V_{1.5}O_{4.75}$ are 54, 85 and 119 Ω, respectively.

Vanadium oxide based cathode materials generally suffer from serious dissolution in aqueous electrolytes, which causes rapid capacity decay upon cycling. To study the dissolution of active materials in electrolyte, the cathode slices are immersed in 3.0 mol/L $ZnSO_4$ aqueous solution, where the dissolution of vanadium based oxides can be told from the color change of the electrolyte (Fig. S9 in Supporting information). After 14 days, the solution with V_2O_5 change into light yellow, suggesting the dissolution of V_2O_5 in aqueous $ZnSO_4$. However, the solution with $Ti_{0.2}V_{1.8}O_{4.9}$ shows a lighter color, suggesting its mitigated dissolution.

Figs. 4a-c show the CV curves of V_2O_5, $Ti_{0.2}V_{1.8}O_{4.9}$, and $Ti_{0.5}V_{1.5}O_{4.75}$ at different scan rates. According to power law equation about the relationship between the current (i) and the scanning rate (v) [54–57]:

$$i = av^b \tag{1}$$

$$log(i) = blog(v) + log(a) \tag{2}$$

where a and b are adjustable parameters. When the value of b is close to 0.5, the electrochemical reaction is diffusion-controlled, while if b is close to 1.0, it indicates a capacitive-controlled process [58,59]. The b values of the four redox peaks for V_2O_5 are in the range of 0.83–1.04, while the b values for $Ti_{0.2}V_{1.8}O_{4.9}$ and $Ti_{0.5}V_{1.5}O_{4.75}$ are in the ranges of 0.78–0.94 and 0.69–0.90, respectively (Figs. 4d-f). The high b values (closed to 1) of all three samples suggest the capacitive-controlled electrochemical processes. With the introduction of Ti, the b value displays a decreasing trend, demonstrating that the Ti doping enhances the diffusion contribution.

To further study the structure transformation of $Ti_{0.2}V_{1.8}O_{4.9}$ during the charge and discharge process, *ex-situ* XPS, *in-situ* XRD, and *in-situ* Raman are conducted (Fig. 5). In discharged state, the high-resolution V 2p spectrum present three components from V(V), V(IV) and V(III) [60,61], with percentages of 23.68%, 61.91%, and 14.36%, respectively. In charged state, only V(V) and V(IV) exist in the sample and their percentages are 49.01% and 50.91%, respectively (Fig. 5a). For the high-resolution Zn 2p spectra, the sample in discharged state show much stronger peaks than that in charged state (Fig. 5b). The results indicate that the Zn^{2+} is inserted into the $Ti_{0.2}V_{1.8}O_{4.9}$ accompanied by the reduction of V species during discharge and the Zn^{2+} is extracted from the material accompanied by the oxidation of V species during charge process.

Fig. 5c presents the *in-situ* XRD pattern, from where the (101), (011) and (301) diffractions are observed at 25.9°, 32.9° and 34.9°. During the discharge/charge processes, the diffraction peaks vary in intensity periodically, while the peak position shows negligible change. The *in-situ* XRD results demonstrate that the Zn^{2+} is intercalated into and extracted from the $Ti_{0.2}V_{1.8}O_{4.9}$ highly reversibly. Fig. 5d presents the *in-situ* Raman spectra. The O-V-O (193, 283

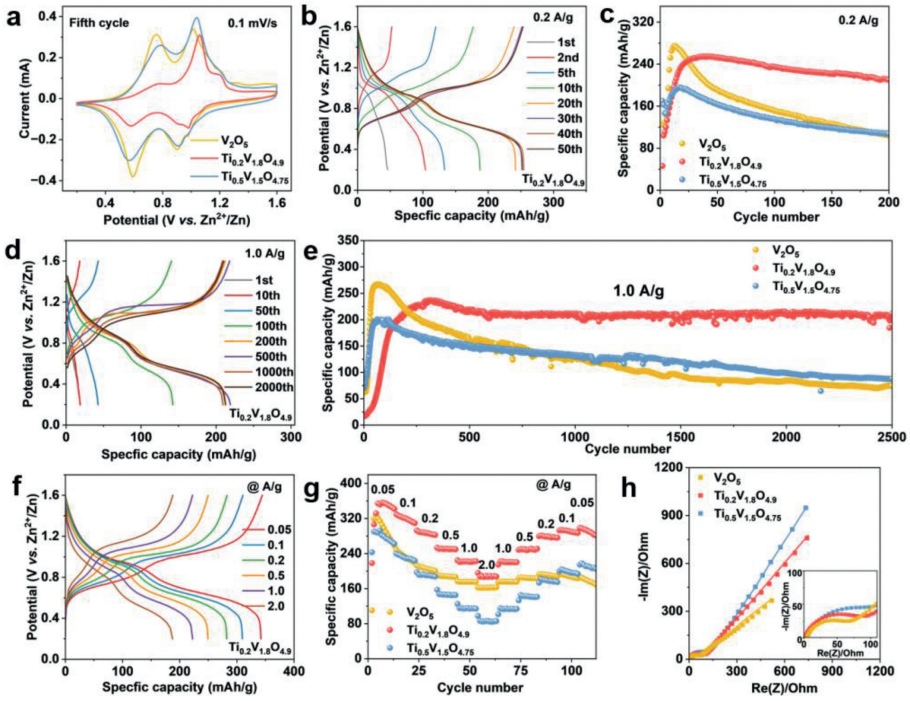

Fig. 3. (a) The 5th cycle CV curves of V_2O_5, $Ti_{0.2}V_{1.8}O_{4.9}$ and $Ti_{0.5}V_{1.5}O_{4.75}$ at 0.1 mV/s. (b) GCD profiles of $Ti_{0.2}V_{1.8}O_{4.9}$ at 0.2 A/g. (c) Cycling performance of V_2O_5, $Ti_{0.2}V_{1.8}O_{4.9}$ and $Ti_{0.5}V_{1.5}O_{4.75}$ at 0.2 A/g. (d) GCD curves of $Ti_{0.2}V_{1.8}O_{4.9}$ at 1.0 A/g. (e) Cycling performances of V_2O_5, $Ti_{0.2}V_{1.8}O_{4.9}$ and $Ti_{0.5}V_{1.5}O_{4.75}$ at 1.0 A/g. (f) GCD curves of $Ti_{0.2}V_{1.8}O_{4.9}$ at different current densities. (g) Rate performances of V_2O_5, $Ti_{0.2}V_{1.8}O_{4.9}$ and $Ti_{0.5}V_{1.5}O_{4.75}$. (h) EIS plots of V_2O_5, $Ti_{0.2}V_{1.8}O_{4.9}$ and $Ti_{0.5}V_{1.5}O_{4.75}$.

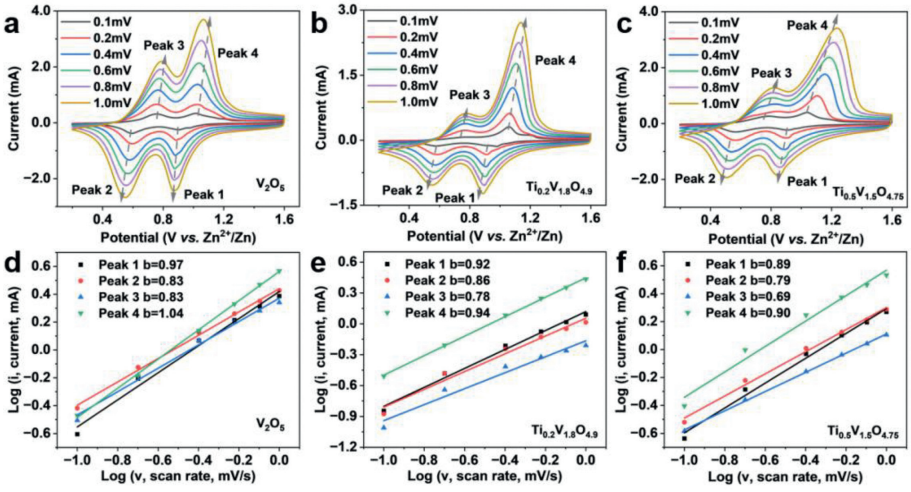

Fig. 4. The CV curves of (a) V_2O_5, (b) $Ti_{0.2}V_{1.8}O_{4.9}$ and (c) $Ti_{0.5}V_{1.5}O_{4.75}$ at different scan rates. log(*i*) *vs.* log(*v*) plots of (d) V_2O_5, (e) $Ti_{0.2}V_{1.8}O_{4.9}$, (f) $Ti_{0.5}V_{1.5}O_{4.75}$.

cm^{-1}), V_3-O (303, 524 cm^{-1}) and V-O-V (478, 697 cm^{-1}) bands weaken gradually during discharge and almost disappear when the potential reaches ~0.87 V and below. During charge, the V_3-O and V-O-V bands reappear when the voltage reach over ~1.2 V. For the V=O bands (994 cm^{-1}), it shows a same regular intensity change and shift towards lower wavenumber slightly during discharge and moves back during charge. The periodic change in the *in-situ* Raman spectra demonstrates the excellent reversibility of $Ti_{0.2}V_{1.8}O_{4.9}$ upon Zn^{2+} intercalation/extraction.

To verify the application potential, a pouch cell was assembled with $Ti_{0.2}V_{1.8}O_{4.9}$ cathode and 3.0 mol/L $ZnSO_4$ electrolyte. It shows a capacity of 236 mAh/g and 95.7% capacity retention after 100 cycles at 0.1 A/g (Fig. S10 in Supporting information). These results demonstrate that doping an appropriate amount of Ti effectively enhances the cycling stability of V_2O_5 cathode materials in aqueous $ZnSO_4$ electrolyte. Considering the good zinc storage performances in both coin cells and pouch cells, the $Ti_{0.2}V_{1.8}O_{4.9}$ cathode material shows a bright application prospect in AZIBs.

In conclusion, we synthesized a series of yolk-shell structured titanium vanadium oxides with different Ti content by a simple spray drying method. Doping 10% of Ti reduces the lattice spacing of V_2O_5 but does not alter the crystal structure. Introducing 25% of Ti leads to the formation of anatase/rutile residue phases. With the doping of an appropriate amount of Ti, the dissolution of V_2O_5 in aqueous $ZnSO_4$ electrolyte can be alleviated, leading to improved cyclability. When employed as the cathode material for ZIBs, the optimized material, $Ti_{0.2}V_{1.8}O_{4.9}$, demonstrates not only high capacity (355 mAh/g) but also ideal cyclability (89% after 2500 cycles, 1.0 A/g) in aqueous $ZnSO_4$ electrolyte. *Ex-situ* XPS, *in-situ* XRD, and *in-situ* Raman characterizations demonstrate

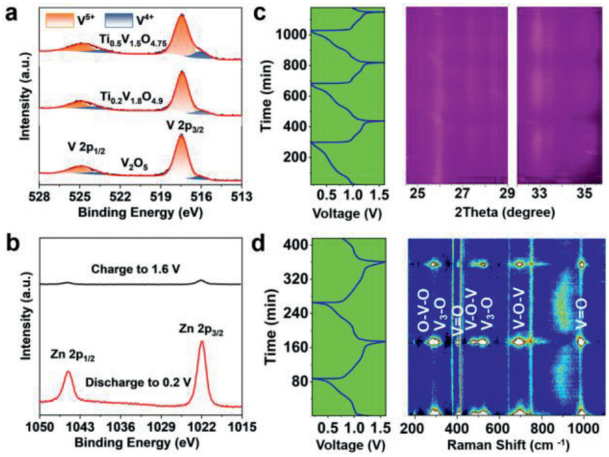

Fig. 5. (a) V 2p and (b) Zn 2p *ex-situ* XPS spectra of the $Ti_{0.2}V_{1.8}O_{4.9}$ recorded at different electrochemical states. (c) *In-situ* XRD pattern and (d) *in-situ* Raman spectra of the $Ti_{0.2}V_{1.8}O_{4.9}$ recorded at 0.1 A/g.

the Zn^{2+} intercalation/de-intercalation is highly reversible in the $Ti_{0.2}V_{1.8}O_{4.9}$. This work provides an effective strategy to mitigate the dissolution issue of cathode material in aqueous electrolytes by transition metal doping.

Declaration of competing interest

The authors declare that they have no known competing financial interests or personal relationships that could have appeared to influence the work reported in this paper.

Acknowledgments

This work was supported by the National Natural Science Foundation of China (No. 52102299), the Independent Innovation Project of Hubei Longzhong Laboratory (No. 2022ZZ-18), the Guangdong Basic and Applied Basic Research Foundation (No. 2021A1515110059), and the Foshan Xianhu Laboratory of the Advanced Energy Science and Technology Guangdong Laboratory (No. XHT2020-003).

Supplementary materials

Supplementary material associated with this article can be found, in the online version, at doi:10.1016/j.cclet.2023.108421.

References

[1] S. Koohi-Fayegh, M.A. Rosen, J. Energy Storage 27 (2020) 101047.
[2] J. Zhu, L. Hu, P. Zhao, et al., Chem. Rev. 120 (2020) 851–918.
[3] D. Kundu, B.D. Adams, V. Duffort, et al., Nat. Energy 1 (2016) 16119.
[4] D. Chao, W. Zhou, F. Xie, et al., Sci. Adv. 6 (2020) eaba4098.
[5] H. Jia, Z. Wang, B. Tawiah, et al., Nano Energy 70 (2020) 104523.
[6] X. Jia, C. Liu, Z.G. Neale, et al., Chem. Rev. 120 (2020) 7795–7866.
[7] X. Zeng, J. Hao, Z. Wang, et al., Energy Storage Mater. 20 (2019) 410–437.
[8] Z. Yang, X. Pan, Y. Shen, et al., Small 18 (2022) 2107743.
[9] X. Wu, Y. Xiang, Q. Peng, et al., J. Mater. Chem. A 5 (2017) 17990–17997.
[10] Y. Liu, X. Wu, Chin. Chem. Lett. 33 (2022) 1236–1244.
[11] B. He, Q. Zhang, L. Li, et al., J. Mater. Chem. A 6 (2018) 14594–14601.
[12] M. Chen, J. Zhang, Y. Dong, et al., Chem. Eng. J. 433 (2022) 134507.
[13] Y. Zhang, F. Wan, S. Huang, et al., Nat. Commun. 11 (2020) 2199.
[14] L. Xing, C. Zhang, M. Li, et al., Energy Storage Mater. 52 (2022) 291–298.
[15] Y. Niu, D. Wang, Y. Ma, et al., Chin. Chem. Lett. 33 (2022) 1430–1434.
[16] Z. Li, B. Wu, M. Yan, et al., ACS Appl. Mater. Interfaces 12 (2020) 10420–10427.
[17] X. Li, H. Cheng, H. Hu, et al., Chin. Chem. Lett. 32 (2021) 3753–3761.
[18] S. Deng, Z. Yuan, Z. Tie, et al., Angew. Chem. Int. Ed. 59 (2020) 22002–22006.
[19] Y.X. Zeng, X.F. Lu, S.L. Zhang, et al., Angew. Chem. Int. Ed. 60 (2021) 22189–22194.
[20] Y. Xue, X. Shen, H. Zhou, et al., Chem. Eng. J. 448 (2022) 137657.
[21] W. Wang, V.S. Kale, Z. Cao, et al., ACS Energy Lett. 5 (2020) 2256–2264.
[22] W. Li, K. Wang, S. Cheng, et al., Energy Storage Mater. 15 (2018) 14–21.
[23] M. Li, Z.L. Li, X.P. Wang, et al., Energy Environ. Sci. 14 (2021) 3796–3839.
[24] W.W. Zhang, C.L. Zuo, C. Tang, et al., Energy Technol. 9 (2021) 2000789.
[25] Y. Wang, Z. Wang, F. Yang, et al., Small 18 (2022) 202107033.
[26] F. Liu, Z. Chen, G. Fang, et al., Nano-Micro Lett. 11 (2019) 25.
[27] Y. Li, Z. Huang, P.K. Kalambate, et al., Nano Energy 60 (2019) 752–759.
[28] X. Chen, L. Wang, H. Li, et al., J. Energy Chem. 38 (2019) 20–25.
[29] Y. Yang, Y. Tang, S. Liang, et al., Nano Energy 61 (2019) 617–625.
[30] R. Li, H. Zhang, Q. Zheng, et al., J. Mater. Chem. A 8 (2020) 5186–5193.
[31] Y. Ma, A. Huang, H. Zhou, et al., J. Mater. Chem. A 5 (2017) 6522–6531.
[32] Y. Dou, X. Liang, G. Gao, et al., J. Alloys Compd. 735 (2018) 109–116.
[33] M. Giorgetti, M. Berrettoni, Chem. Mater. 19 (2007) 5991–6000.
[34] Y. Liu, J. Xu, J. Li, et al., Coord. Chem. Rev. 460 (2022) 214477.
[35] G. Zhang, T. Wu, H. Zhou, et al., ACS Energy Lett. 6 (2021) 2111–2120.
[36] G.D. Cui, Y.X. Zeng, J.F. Wu, et al., Adv. Sci. 9 (2022) 9.
[37] W. Yang, W. Yang, Y. Huang, et al., Chin. Chem. Lett. 33 (2022) 4628–4634.
[38] M. Du, F. Zhang, X. Zhang, et al., Sci. China Chem. 63 (2020) 1767–1776.
[39] J. Zhou, L. Shan, Z. Wu, et al., Chem. Commun. 54 (2018) 4457–4460.
[40] Y. Sun, Z. Xu, X. Xu, et al., Energy Storage Mater. 48 (2022) 192–204.
[41] F. Huang, X. Li, Y. Zhang, et al., Adv. Mater. 34 (2022) 2203710.
[42] M. Neelima, S. Vandana, A. Kathirvel, et al., Optik 252 (2022) 168516.
[43] S. Phatyenchuen, B. Pongthawornsakun, J. Panpranot, et al., J. Environ. Chem. Eng. 6 (2018) 5655–5661.
[44] Q. Fu, A.L. Hansen, B. Schwarz, et al., Chem. Mater. 34 (2022) 9844–9853.
[45] A. Baltakesmez, C. Aykaç, B. Güzeldir, Appl. Phys. A 125 (2019) 441.
[46] S. Zhu, S. Chen, H. Zhang, et al., Ionics 28 (2022) 2931–2942.
[47] S. Qiu, L. Xiao, X. Ai, et al., ACS Appl. Mater. Interfaces 9 (2017) 345–353.
[48] M. Yan, P. He, Y. Chen, et al., Adv. Mater. 30 (2018) 1703725.
[49] X.W. Wang, L.Q. Wang, B. Zhang, et al., J. Energy Chem. 59 (2021) 126–133.
[50] P.J. Wang, X.D. Shi, Z.X. Wu, et al., Carbon Energy 2 (2020) 294–301.
[51] N. Zhang, Y. Dong, M. Jia, et al., ACS Energy Lett. 3 (2018) 1366–1372.
[52] Y. Dong, M. Jia, Y. Wang, et al., ACS Appl. Energy Mater. 3 (2020) 11183–11192.
[53] P. Hu, T. Zhu, J. Ma, et al., Chem. Commun. 55 (2019) 8486–8489.
[54] M. Narayanasamy, B. Kirubasankar, M. Shi, et al., Chem. Commun. 56 (2020) 6412–6415.
[55] F. Liu, Math. Inequal. Appl. 22 (2019) 25–44.
[56] H. Wang, C. Zhu, D. Chao, et al., Adv. Mater. 29 (2017) 1702093.
[57] T. Brezesinski, J. Wang, S.H. Tolbert, et al., Nat. Mater. 9 (2010) 146–151.
[58] J. Wang, J. Polleux, J. Lim, et al., J. Phys. Chem. C 111 (2007) 14925–14931.
[59] H. Lindström, S. Södergren, A. Solbrand, et al., J. Phys. Chem. B 101 (1997) 7717–7722.
[60] X. Zhang, F. Xue, X. Sun, et al., Chem. Eng. J. 445 (2022) 136714.
[61] J. Zhang, S. Liu, H. Liu, et al., J. Alloys Compd. 920 (2022) 166010.